



Microstructure and mechanical properties of 316L austenitic stainless steel processed by different SLM devices

A. Röttger¹ · J. Boes¹ · W. Theisen¹ · M. Thiele² · C. Esen² · A. Edelmann³ · R. Hellmann³

Received: 30 September 2019 / Accepted: 28 April 2020 / Published online: 22 May 2020
© The Author(s) 2020

Abstract

In this work, we examined the influence of different types of selective laser melting (SLM) devices on the microstructure and the associated material properties of austenitic 316L stainless steel. Specimens were built using powder from the same powder batch on four different SLM machines. For the specimen build-up, optimized parameter sets were used, as provided by the manufacturers for each individual SLM machine. The resulting microstructure was investigated by means of scanning electron microscopy, which revealed that the different samples possess similar microstructures. Differences between the microstructures were found in terms of porosity, which significantly influences the material properties. Additionally, the build-up direction of the specimens was found to have a strong influence on the mechanical properties. Thus, the defect density defines the material's properties so that the ascertained characteristic values were used to determine a Weibull modulus for the corresponding values in dependence on the build-up direction. Based on these findings, characteristic averages of the mechanical properties were determined for the SLM-manufactured samples, which can subsequently be used as reference parameters for designing industrially manufactured components.

Keywords Selective laser melting · Austenitic stainless steel · Additive manufacturing · 316L · Laser powder bed fusion

1 Introduction

Processing of steels by additive manufacturing (AM) has gained importance in recent years. This can be attributed to both the feasibility of processing prototypes or individually developed component parts within a short time and to the absence of development times [1]. In addition, AM can be considered as a material-saving technology because of a potential recycling of the feedstock (for example, reuse of unmelted metal powder during selective laser melting) [2, 3]. Furthermore, only a small amount of post-processing (polishing, sand-blasting, heat treatment) of additively manufactured components is necessary, so that cost-

intensive value-added processes can be reduced to a minimum [4]. For the processing of metals, a laser or an electron beam can be used as the energy source, allowing partial or full melting of the feedstock powder. In this work, we are focusing on selective laser melting (SLM). For further information on processing of metals by electron beam melting (EBM) or selective laser sintering (SLS), we therefore refer to the literature [5, 6]. Selective laser melting is an iterative process, consisting of three main steps: (1) application of a 30- to 50- μm -thick powder layer on a building platform; (2) partial melting of the powder bed by a laser source based on previously imported 3D-CAD data; and (3) lowering of the building platform and restarting at (1). The powder is usually applied by a polymer or rubber scraper.

Research within the last two decades mainly focused on the process control, including the effect of different process parameters on process stability and the resulting microstructure and material properties [7–9]. The development of new materials, the necessary investigation of appropriate processing parameters for these new materials, and post-processing (HIP treatment, machining) of SLM-densified components [10, 11] also have to be mentioned. Besides experimental approaches, also physics-based simulations were developed

✉ A. Röttger
roettger@wtech.rub.de

¹ Materials Department, Ruhr University Bochum, Universitätsstraße 150, 44801 Bochum, Germany

² Applied Laser Technologies, Ruhr University Bochum, Universitätsstraße 150, 44801 Bochum, Germany

³ Applied Laser and Photonics Group, University of Applied Sciences Aschaffenburg, Würzburger Str. 45, 63743 Aschaffenburg, Germany

for the reproduction and optimization of AM processes. These investigations provide insight into complex aspects dominating powder bed-based laser additive manufacturing processes, such as powder bed density and powder flow behavior or heat flux and temperature distribution [12–15]. Furthermore, simulative investigations were conducted on the formation of defects and microstructure during these processes [16–19]. SLM devices have become market-ready in terms of their functionality and efficiency for manufacturing prototypes and complex-shaped component parts, dental parts, and propellers [20]. For the production of parts, the optimum and material-specific process parameters for the respective SLM device are often used, as provided by the SLM-device manufacturer. A variety of material properties for SLM-manufactured specimens has been gathered by many laboratory-scale investigations and has been published. These investigations often made use of own optimized process parameters so that these values do not necessarily reflect the achievable values in the industrial SLM process. In this context, the influence of the building direction of SLM-processed 316L steel was investigated by Mertens et al. and Delgado et al., who found better material properties for specimens built in a horizontal arrangement compared with specimens built vertically [21, 22]. The influence of a further post-treatment on the material properties was investigated by Löber et al., and the effect of the scanning strategy was characterized by Rasch et al. [23, 24].

It is well known that the strength of SLM-manufactured samples exceeds the strength of the same material produced by casting or hot-isostatic pressing. However, the elongation values of austenitic stainless steel 316L manufactured by SLM are lower than those of cast or sintered 316L. The lower elongation values are attributed to microstructural defects such as pores, cracks, or binding defects. These microstructural defects strongly influence the material properties [25]. The material properties of SLM-manufactured components are influenced by the scanning strategy, the choice of optimal process parameters, the SLM system itself, the powder feeding system, and the powder properties. In recent years, both the technology as well as the process parameters for SLM devices have been optimized allowing for the production of components with a porosity lower than 1%. However, there is an open question as to whether the use of different SLM devices and the respective optimized process parameters for each device lead to comparable part properties, in terms of microstructure and mechanical strength. In addition, there is no adequate material data that can be used for the structural design of mechanical structural components.

The aim of this investigation is, on the one hand, to determine the influence of different SLM devices on the microstructure and the associated material properties. On the other hand, a statistical evaluation of the measured values was carried out to provide material data for the constructive design of

SLM-manufactured parts. For this purpose, 316L stainless steel powder was processed by four different SLM devices. In order to eliminate the influence of the powder properties (chemical composition, flow properties etc.), only powder from one powder batch was used. The specimens were built using the optimized process parameters, as provided by the SLM machine manufacturers for each individual machine. These parameters were evaluated for the production of parts with a maximum density and simultaneously low sample distortion. The use of the optimized parameters is therefore assumed to lead to the good results in terms of specimen density and overall quality for each used SLM machine. Furthermore, the use of the optimally determined process parameters of the SLM-device manufacturers enables transferability to the industrial process. The resulting microstructure was investigated by means of scanning electron microscopy, and the porosity was determined by quantitative image analysis. Subsequently, tensile tests were carried out allowing for a discussion of the mechanical properties with respect to the microstructure. Finally, the mechanical characteristic values were statistically evaluated to provide meaningful values for a mechanical design of SLM-manufactured components, depending on the construction direction. Thus, this work aims to contribute to a technologically orientated discussion on the mechanical properties of SLM-built parts made of stainless steel 316L.

2 Materials and methods

2.1 Materials

In this work, grade 316L austenitic stainless steel (1.4404; X2CrNiMo18-12-2) was used in the gas-atomized condition. The used powder was provided by Deutsche Edelstahlwerke GmbH. Different SLM machines were used in this work, whereas all SLM build cycles were performed using powder from the same powder batch. With this approach, the influence of the powder properties was kept constant throughout the entire investigation. As a reference material, AISI 316L steel in the hot-rolled and solution-annealed condition was used. The chemical composition of the steel powder and the reference material was measured by energy dispersive spectrometry (EDS) and optical emission spark spectrometry (OBLF QSN 750-II), respectively. The results are listed in Table 1.

2.2 Powder analysis

The particle size and shape of the powder were analyzed by scanning electron microscopy (SEM). The particle size distribution and the average particle size were determined by laser diffraction in accordance with ISO 13320 using a Mastersizer 2000 (Malvern Instruments

Table 1 Sample designation and chemical composition of the materials measured by optical emission spectroscopy (SLM-densified) and energy disperse spectrometry (powder) in mass%

Sample	Processing	C	Cr	Ni	Si	Mo	Mn	Fe
316L powder	Starting powder	–	16.69	12.57	1.22	2.63	0.03	bal.
316L cast	Cast material	0.014	17.43	11.67	0.37	2.30	0.80	bal.
Nominal composition	–	max. 0.03	16.50–18.50	10.50–13.00	–	2.00–2.50	–	bal.

The amount of carbon could not be measured quantitatively by EDS. Therefore, no value is provided

Ltd.) The flowability of the powder was evaluated by measuring the apparent density with respect to DIN ISO 697, and the powder flow rate was measured using a Hall flowmeter in accordance with DIN EN ISO 4490. The flow rate was measured at a temperature of 22.4 °C and a relative air humidity of 50.3%. For each value, three measurements were performed and the average mean as well as the standard deviation was calculated.

2.3 SLM processing

In this work, four SLM machines from different manufacturers were used for the manufacturing of specimens. The microstructure and the associated material properties of the produced specimens characterized and the results from the different SLM machines were compared with each other. It should be highlighted here that the intention of this work is not to provide a benchmark of the used SLM machines in terms of their performance. With this work, the differences in mechanical properties of the same material built by different SLM devices are investigated. For this reason, only the essential process parameters are provided in Table 2, so that no identification of used SLM machines is possible based on the process parameter choice. The individual machines are referred to as device A to device D. The sample designation is based on the used SLM device and consists of two letters: the first letter (A to D) indicates the SLM device, and the second letter (v = vertical, h = horizontal) denotes the built-up direction. As process parameters, the optimal parameters for the material 316L provided by the

manufacturers of the respective machines (see Table 2) were used. The employed machines possess different powder supply systems (linear as well as circular recoater movement and step-wise as well as continuous powder supply). All SLM devices possess an Yb-fiber laser with a wavelength of approximately 1070 nm. The applied laser power varied in the range of 100 to 400 W. The laser energy given in Table 2 refers to the measured laser energy on the building platform, which is lower than the maximum laser energy due to optical losses. SLM build-up was performed on a base plate made of an austenitic stainless steel 1.4301 (X5CrNi18-10). Tensile specimens were manufactured horizontally and vertically to the base plate, as shown in Fig. 1. In order to characterize the microstructures, smaller samples were taken from the tensile samples, as shown in Fig. 1a.

The sample build-up was performed using different scanning strategies. The data given in Table 2 relate to the displacement angle between two successively applied layers. Thus, a value of 90° indicates a perpendicular movement of the laser with respect to the laser direction of the previously densified layer. The energy input per unit length E_L and energy density E_D were calculated using Eq. 1 and Eq. 2 with the exposure time t_E , the point distance p_D , the effective laser power P_{eff} , the hatch distance H_D , and the layer thickness l_T .

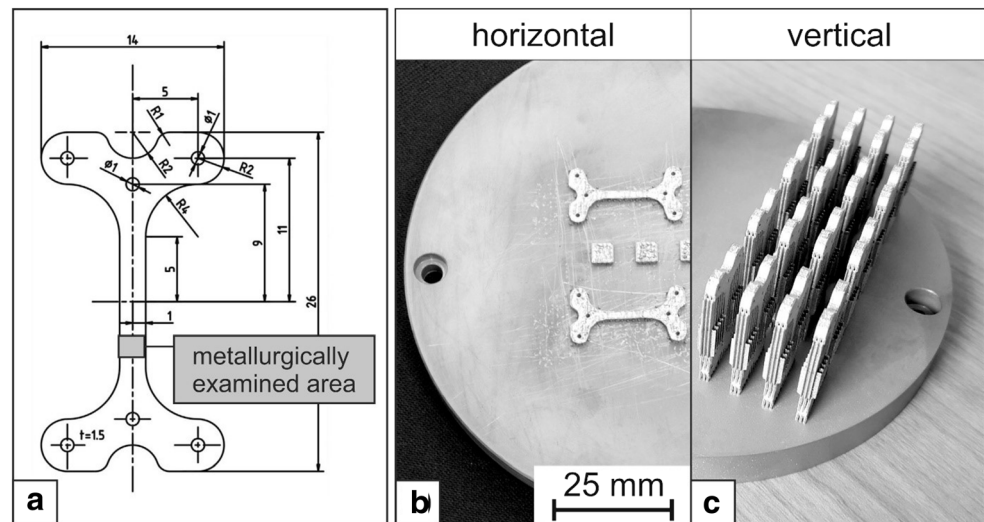
$$E_L = \frac{t_E}{p_D} \cdot P_{eff} \tag{1}$$

$$E_V = \frac{t_E}{p_D} \cdot \frac{P_{eff}}{H_D \cdot l_T} \tag{2}$$

Table 2 Process parameters depending on the respective SLM system. The process parameters are the optimal parameters given by the manufacturer of the respective SLM system

Device designation	Laser power, P_{eff} [W]	Laser spot size [μm]	Base plate temperature [$^{\circ}\text{C}$]	Layer thickness l_T [μm]	Scanning velocity [mm/s]	Hatch distance H_D [μm]	Scanning strategy (tilt of x to y)	Energy input per unit length, E_L [J/m]	Energy density, E_V [J/mm ³]	Recoater movement
A	136.1	100	80	40	928.1	100	90	146.6	0.0365	Linear
B	73.5	90	no	30	300.0	30	90	245.0	0.2722	Circular
C	148.8	80	no	45	888.9	80	10	167.4	0.0465	Linear
D	114.4	90	50	50	1000.0	100	90	114.4	0.0229	Linear

Fig. 1 Tensile specimen. **a** Technical drawing of the constructed tensile specimens. Arrangement and orientation of the samples on the base plate: **b** horizontal and **c** vertical build-up



2.4 Metallography and microscopy

For microscopic investigations, SLM-processed specimens were cut by a cBN cutting disk. Cut specimens were further embedded in an electrically conductive resin and ground with SiC paper (320→800→1000 mesh size) and polished with diamond suspensions with an average diamond particle diameters of 9 μm , 6 μm , 3 μm , and 1 μm . Finally, the surface was finished by polishing with an oxide polishing solution (0.25 μm). The microstructure was contrasted by etching with NITAL solution and was then investigated by scanning electron microscopy (SEM) using a MIRA 3 GM from Tescan in secondary-electron contrast mode. For SEM investigations, an acceleration voltage of 15 keV and a working distance of 15 mm were used. The specimen porosity was measured using optical microscopy (OM). OM images were binarized and the area proportions of pores were determined with the help of quantitative image analysis using the software Image J (version 1.49v). For each specimen, five different OM images were analyzed and the average mean porosity value was calculated.

2.5 Mechanical testing

To evaluate the material's strength with respect to the used SLM device, tensile testing was performed in accordance with DIN EN ISO 6892-1:2009-12 at a Zwick Roell Z100 universal testing machine. For this purpose, our designed tensile specimens, as shown in Fig. 1a, were manufactured in both vertical and horizontal directions. Before testing, the surfaces of the tensile specimens were ground, in order to avoid premature failure

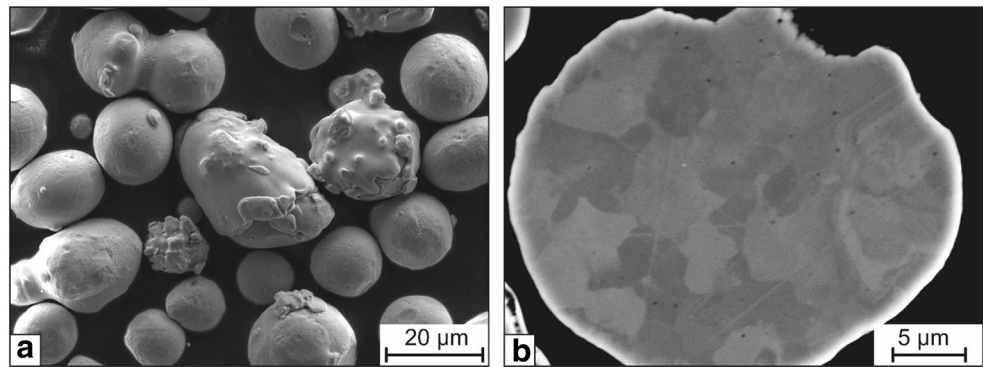
because of high stresses due to stress concentration at the uneven specimen surface. The specimens were tested until rupture using a constant crosshead speed of 0.5 mm/min. The elongation of the tensile specimens during testing was measured by an extensometer, and the applied force was determined simultaneously with a 10 kN load cell.

3 Results and discussion

3.1 Powder characterization

Before processing, the steel powder was sieved into a fraction of +20 to $-63\ \mu\text{m}$, and the sieved powder was analyzed in terms of particle shape, particle size, and chemical composition. The morphology of the steel powders is shown in Fig. 2 both as an overview (Fig. 2a) and as a cross-section (Fig. 2b). The powder particles possess a size between +20 and $-63\ \mu\text{m}$, and the d_{10} and d_{90} values were determined to be 25 μm and 56 μm , respectively (see Table 3). The d_{50} -particle size was determined to be 38 μm . The powder particles have a spherical shape with a small amount of satellites. The presence of satellites is attributed to the gas atomization process: small powder particles adhere to bigger ones due to different flow conditions, crystallization rates, and pronounced particle interactions between liquid and solid steel droplets [26]. Due to the spherical shape and small amount of satellites, the powder showed a good flowability with a flow time of $13.93 \pm 0.11\ \text{s}$ in the Hall-flow test, and a bulk density of $4.34\ \text{g/cm}^3$. Within the powder microstructure, depending on particle size, grains with a size of 1 to 15 μm are present. Smaller grains are mainly present in smaller powder particles, which is due to the higher crystallization rate during the gas atomization.

Fig. 2 Investigated powder particles of steel 316L used for SLM processing. **a** SLM image for the description of the powder morphology. **b** Microstructural cross-section of a powder particle



3.2 Description of the microstructure and the defects in SLM-processed samples from 316L

The microstructure of the SLM-densified 316L steel processed by the four different devices A to D is depicted in Fig. 3. The microstructure must be described using different scale sizes, hereinafter referred to as the meso- and microscale. At lower magnification, i.e., on the mesoscale, the microstructure is characterized by a layer-wise morphology. The layer thickness is about 10 to 55 μm , which corresponds to 33 to 68% of the thickness of the powder bed (30–80 μm) previously applied by the recoater-system. By an optimal powder application, the ratio between the applied layer thickness of the powder bed and the SLM-compacted layer thickness is determined by the bulk density. The bulk density was measured to be 4.34 g/cm^3 , whereby the density of 316L steel is 7.9 g/cm^3 , so that a packing density of about 55% is present in the applied powder bed before it is remelted by the laser. No pronounced microstructural differences are observed between the specimens' microstructures, regardless of the SLM device used.

Grains having a size of 10 to 50 μm are visible within the etched microstructure. It seems that one grain can extend over two consecutive layers, as indicated in Fig. 4. This behavior is attributed to epitaxial growth of the grains [27]: the grains orient themselves during solidification according to the orientation of the solid nucleus surface (surface of the previously applied layer), which is the energetically favored surface for crystallization [28]. However, the heat flux influences the growth direction of the grains, resulting in grain growth perpendicular to the previously applied layers. During solidification, isolated grains grow towards the melt pool center. When

the grains reach a certain size, their surfaces meet and form grain boundaries. If there is an insufficient amount of residual melt between the grains that are moving towards each other, pores and binding defects may be formed [7]. Within the individual grains, smaller cells are forming on the microscale, as depicted in Fig. 4. These present cells will be referred to as subdomains and are characterized by a core/shell-like morphology. In the SEM microstructure, the shell regions in the subdomains appear brighter than the core areas. This indicates that heavy elements, such as Mo, are enriched within the shell region, as evidenced by the work of Prashanth et al. [29]. Local accumulation of these heavy elements can be attributed to the high solidification rate and the associated effects of constitutional undercooling. In the work of Zhong et al., it was shown that the element Mo, in particular, accumulates in the residual melt during solidification of steel 316L [30]. Additionally, the shell regions were found to possess a high dislocation density [31]. Adjacent cell cores can reveal slightly different crystallographic orientations and the cell shells can therefore be understood as low-angle grain boundaries [8, 32]. Despite being widely reported, the interaction between solute atoms and dislocation in these areas are discussed controversially. The cell size is also controlled by the solidification rate, which depends on the time/temperature history during SLM processing. On this account, bigger subdomains are present at the respective boundary surfaces on the individually applied layer. Due to the application of new layers upon solidified layers, additional heat is inserted into the solidified layers, which can represent an in situ heat treatment [33]. Due to the temporally increased temperature, diffusion of atoms and dislocation movement can occur. Thus, the temperature input induced by the melting of subsequent layers is considered an important influence on the microstructure and the properties of SLM-built materials [34]. To summarize, regardless of the selected SLM device, all examined microstructures of the respective specimens are similar with respect to their grain size, layer thickness, substructure morphology, and grain orientation. Based on the microstructural investigations, it can be concluded that, despite the use of different SLM devices, similar laser/powder bed interactions and resulting melting and

Table 3 Measured powder properties

Steel powder	Flow rate [s]	Bulk density [g/cm^3]	Particle size [μm]		
			d_{10}	d_{50}	d_{90}
316L	13.93 ± 0.11	4.34	25	38	56

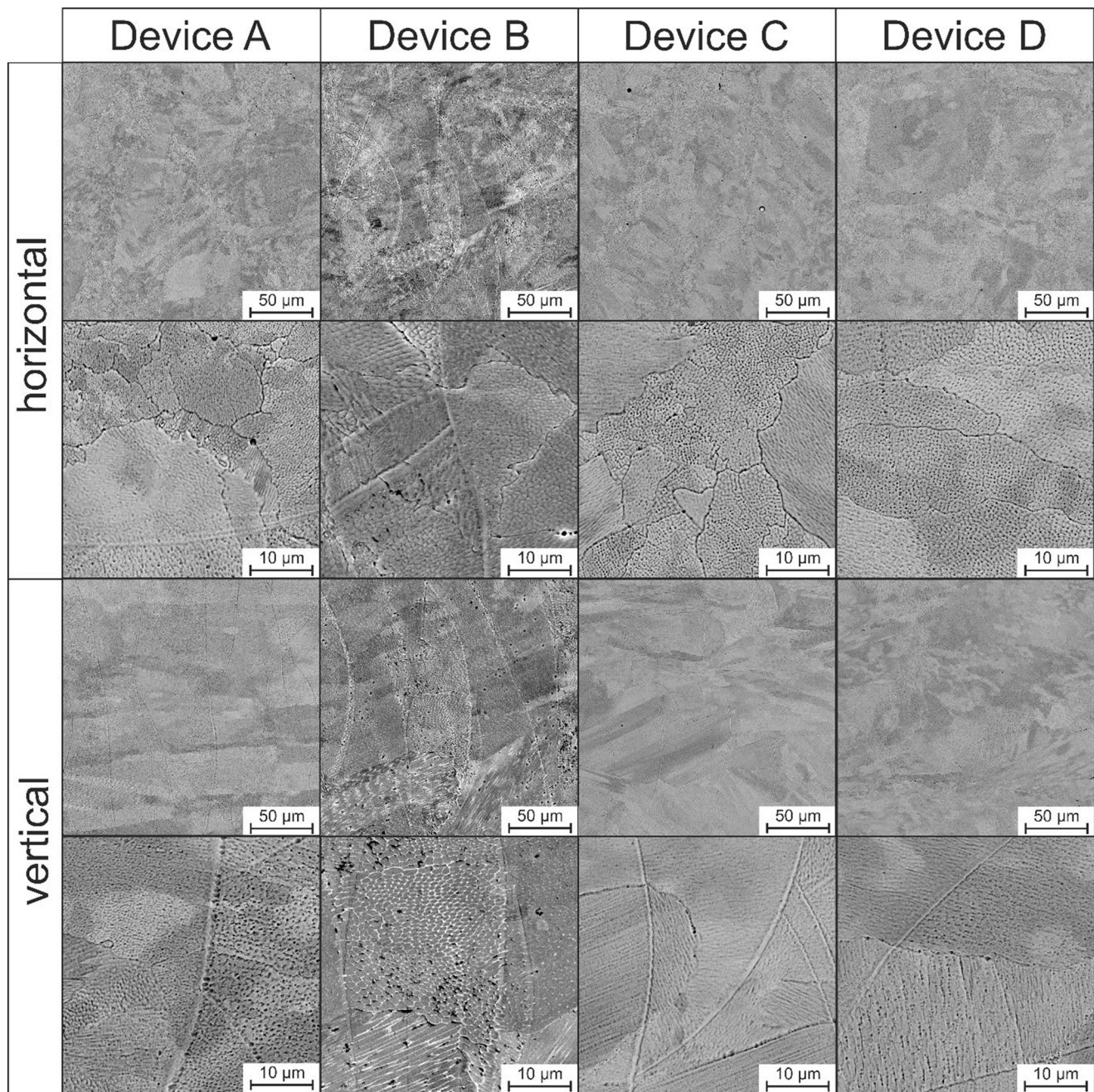


Fig. 3 Microstructure of the 316L processed by different SLM devices with respect to the built-up direction

solidification conditions of the material existed during SLM processing. However, characteristic differences between the individual microstructures built by different SLM devices are found in the porosity, which was determined by quantitative image analysis and is listed in Table 4. The porosity of all specimens is below 1%. The highest porosity was found in the microstructure of the samples manufactured with SLM device B. In contrast, specimens produced with the SLM device A have the lowest porosity of less than 0.03 ± 0.02 vol.-%, independent of the building direction. The specimens manufactured by SLM devices C and D have a porosity of

0.049 to 0.107 vol.-% and lie within the aforementioned extremes. The porosities determined here correspond to characteristic values for the porosity of SLM-built components, which also coincides with the work of others [35, 36].

The pores and cavities that can be observed occasionally in the SLM-built specimens can be a result of several different formation mechanisms. A small fraction of the occurring cavities possesses a spherical and regular shape, indicating their nature as gas pores. Liverani et al. attribute the presence of these defects to the rapid solidification and the simultaneously low solubility of the process gas argon in the steel matrix. Due

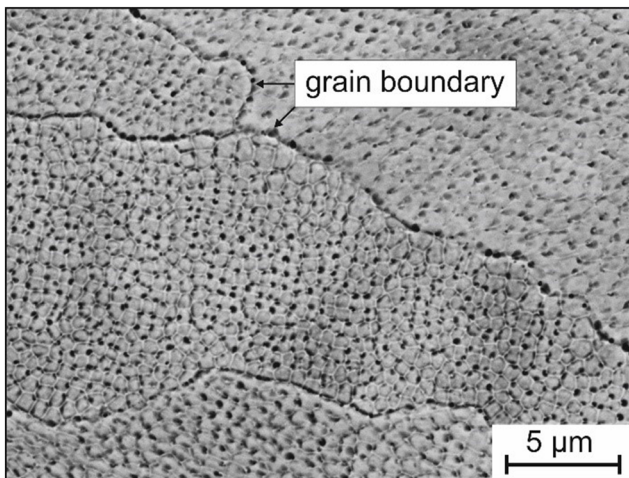


Fig. 4 Substructure of SLM-densified material consisting of coarser grains in which a cell-like substructure is present

to the low solubility in both the molten steel and the solid metal matrix, the argon previously present in the powder bed can only escape in the form of ascending gas bubbles. Because of the rapid solidification rate, only a short time remains for the process gas to escape from the molten metal, so that gas pores remain in the solidified microstructure. Similar to this phenomenon, Yi et al. could show the formation of pinholes during the impact and solidification of metal droplets on rough surfaces [37]. Besides pores which appear to be associated with gas entrapment, binding defects can be found in the SLM-built specimens. As mentioned before, binding defects can occur due to an insufficient amount of residual melt between two adjacent solidification fronts. Furthermore, an insufficient energy input due to poor removal of by-products from the laser-powder interaction zone by the protective gas flow is reported in literature and can be the reason for lack-of-fusion defects [38]. The works of Matthews et al. and Yadroitsev et al. indicate that denudation of powder particles from single hatches can induce void formation by creating spaces with locally low powder bed density [39, 40]. The powder bed density was identified as a crucial influence on the specimen density due to void formation in the work of Ali et al. [41]. In this context, the recoater movement was found to affect the local powder bed density, strongly. Similarly, variations in the powder layer thickness can be seen as a possible reason for the formation of cavities [42]. In our work, uniform and dense microstructure could be produced independently of the used SLM devices in all conducted experiments. Nonetheless, binding defects can be found primarily between two adjacent layers. These defects indicate an insufficient powder bed density. Especially in the case of the specimens built on SLM machine B, the powder feed system could not ensure the application of a homogenous powder layer with a maximum powder bed density. The irregular and locally

occurring insufficient powder distribution is assumed to be the reason for the higher porosity in specimens built by SLM device B.

3.3 Influence of the built-up direction and the SLM-device on the mechanical properties of 316L stainless steel

The motivation of this work was to illustrate the influence of different SLM devices on the formation of the microstructure and the resulting material properties. The same steel powder was used for the SLM-manufacturing of all specimens so that only the machines' influence on the microstructure and the material properties becomes apparent. In this study, we used the respectively optimized SLM processing properties as determined by the SLM-machine manufacturer, so that the results obtained here are directly related to the properties of industrially manufactured SLM components. The used SLM exposure parameters used (see Table 2) represent an optimal set of parameters with which dense specimens with low distortion and good mechanical and chemical properties can be produced. In our own parameter studies (see for a selected SLM-device [43, 44]), we found that the parameters mentioned by the SLM-machine manufacturers representing an optimal parameter set. However, because we do not want to carry out a benchmark between the individual systems and the associated material properties, we deliberately do not indicate the SLM systems used.

Representative stress/strain curves of the produced tensile specimens in the horizontal and vertical build-up directions are shown in Fig. 5, and the corresponding values are listed in Table 4. The overall result is that the yield strength and the tensile strength of SLM-manufactured components are higher in the horizontal build-up direction than in the vertical build-up direction. The reason for this behavior is attributed to the orientation of the layers, the effect of binding defects, and force transmission within the specimen during tensile testing. In the case of vertical build-up, the force is transmitted perpendicularly to the layered structure so that binding defects have a strong influence on the force transmission. Binding defects or pores reduce the specimen's cross-section and represent internal stress concentrations, thus promoting premature failure. In contrast, binding defects neither drastically reduce the load-bearing cross-section of the specimen nor does force transmission take place via these structural defects in the case of specimens that have been built-up horizontally. The same conclusion can be gathered by the work of Deev et al. [45]. The total difference in the yield strength of all measured samples produced by the various SLM devices is 79 MPa. The difference in the tensile strength of all specimens is about 119 MPa. It is clear from the results that, despite the same material was processed with different SLM devices, there are large fluctuations in the resulting strength values. It

Table 4 Results and characteristic values of the tensile tests of the specimens in consideration of the SLM device, built-up direction, and sample porosity

Specimen	Young's modulus [GPa]	Yield strength, Rp0.2 [MPa]	Tensile strength, Rm [MPa]	Uniform elongation Ag [%]	Elongation at fracture A [%]	Specific fracture energy [J/cm ²]	Porosity [%]
Av	182.7 ± 0.11	452.7 ± 9.1	548.8 ± 7.2	41.1 ± 6.7	56.3 ± 7.2	305.5 ± 39.2	0.028 ± 0.021
Ah	165.1 ± 0.54	503.1 ± 32.4	644.3 ± 6.7	32.4 ± 2.4	51.4 ± 9.7	322.8 ± 50.6	0.028 ± 0.021
Bv	164.0 ± 0.00	438.9 ± 3.5	525.1 ± 15.0	11.1 ± 3.5	15.5 ± 2.9	80.7 ± 17.4	0.660 ± 0.340
Bh	167.0 ± 0.00	440.2 ± 21.5	573.5 ± 18.8	31.9 ± 4.3	38.5 ± 4.4	208.4 ± 27.5	0.570 ± 0.100
Bh-HT	205.0 ± 0.00	208.8 ± 13.5	486.4 ± 65.1	44.9 ± 12.7	51.0 ± 13.0	215.4 ± 82.3	0.600 ± 0.900
Cv	150.3 ± 0.35	424.2 ± 8.5	528.9 ± 31.6	31.9 ± 4.3	38.5 ± 4.4	163.2 ± 72.8	0.049 ± 0.041
Ch	153.8 ± 0.07	445.7 ± 23.4	629.8 ± 31.5	35.2 ± 5.4	46.1 ± 8.0	287.1 ± 63.0	0.107 ± 0.051
Dv	142.0 ± 0.22	458.5 ± 13.7	598.8 ± 1.0	45.9 ± 4.5	63.2 ± 0.7	361.3 ± 13.5	0.073 ± 0.029
Dh	141.2 ± 0.17	469.6 ± 4.7	621.2 ± 6.7	31.5 ± 0.7	48.5 ± 0.4	290.3 ± 5.6	0.089 ± 0.045
Reference 316L [35]	No data	500	590	No data	No data	No data	~ 0
Reference 316L cast [36]	190–200	365 ± 22	563 ± 6	46.7	69 ± 9	365.0 ± 57	~ 0

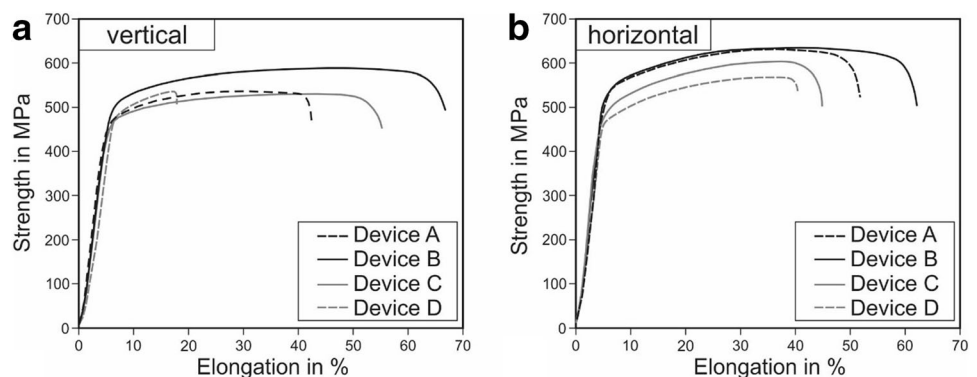
h horizontal; *v* vertical

can therefore be stated, that—from a technological point of view—the use of optimized parameters does not necessarily result in comparable and good mechanical properties. Possible reasons for this can be but are not limited to differences concerning the powder supply or protective gas flow characteristics [38, 42]. Nevertheless, the yield strength of the SLM-densified specimens exceed those of the reference material 316L in the cast condition. Although the grains on the SLM-built specimens have a size of 10 to 50 μm, the increased yield strength can be attributed to the Hall-Petch relation with respect to the fine-grained substructure within the bigger grains. The substructure, which consists of fine subgrains with a high density of small-angle grain boundaries, represents an effective resistance to dislocation gliding. In this context, the interaction of the high dislocation density and the accumulation of Mo and Si in the interdendritic regions is discussed controversially in literature, but could be considered a further contribution to the material's strength [31]. In addition, tensile strength values can be taken from the SLM-manufactured samples

which are at least at the level of the reference sample in the cast condition. Thus, it can be stated that SLM-manufactured components correspond to the strength level of components in the cast state, independent of the different SLM devices used in this work.

Without consideration of the Ah sample, Young's modulus seems less to be influenced by the build-up direction and has a value of 141 to 182 GPa. Young's modulus in all SLM-densified specimens is about 18 to 59 GPa lower than that of the reference sample in the cast condition. These findings are in agreement with the work of Merkt et al. and Yadroitsev et al. [8, 46], who found a Young modulus of 140 to 220 GPa. In contrast, Hitzler et al. found that Young modulus, tensile strength, and elongation at fracture depend on the sample build-up direction [47]. The work of Niendorf et al. also confirm a directional dependence of the modulus of elasticity as a function of the build-up direction and the laser energy used [48]. EBSD investigations revealed a more or less regular crystallographic orientation of the grains having a slight

Fig. 5 Tensile stress/strain curves of **a** vertical build-up SLM specimens and **b** horizontal build-up SLM specimens



tendency to be orientated in the 011 direction if the samples were built by SLM using a laser power of 400 W [49]. In comparison, the grains were preferentially oriented in the 001 direction in the case of a laser energy of 1000 W. In fcc systems, the 001 direction has the lowest Young's modulus for austenitic steels, thus a preferred orientation of the grains in the 001 direction is accompanied by a lowered Young's modulus [48]. Although the different microstructures show a slight preference with respect to the grain orientation because of their epitaxial growth, the reduced Young's modulus cannot be discussed here on the basis of grain orientation alone. Losertová et al. investigated the effect of a certain porosity of 5 vol.% on the mechanical properties of SLM-manufactured Ti6Al4V alloy. They found a decrease in the strength and an increase in the elastic and plastic properties if a heat treatment was performed. On this account, a low Young's modulus of 54 GPa was found, in contrast to the Young modulus of 110 GPa reported for the cast reference material Ti6Al4V [50]. Capek et al. investigated the material properties of SLM-manufactured, highly porous samples of 316L. With respect to their aimed application of producing scaffold bodies having bone-like properties, a porosity of 87 vol.% was necessary to achieve the low Young's modulus of 0.15 GPa [51]. The effect of porosity on the Young modulus of SLM-densified Co-base alloy was investigated by the work of Jouget et al. [52]. They found a nearly linear relationship; thus, the Young modulus decreases in the direction of a higher porosity. However, the low Young's modulus here has to be discussed with respect to the higher dislocation density and the previously described segregation effect in addition to the porosity and the effect of grain orientation. The higher dislocation density in SLM-processed samples is attributed to the high cooling rates, which is consistent with the work of Saeidi et al., who conducted TEM investigations on SLM-compacted samples made of 316L steel [53]. They found a high dislocation density at the outer areas of the cell structure on the microscale. This area corresponds to the area with the maximum segregation of the element Mo. Benito et al. investigated the change in the Young modulus of cold-deformed pure iron by tensile testing [54]. They examined the evolution of the dislocation density as a function of the deformation condition and found a reduction in the Young modulus by 4 to 7% if tensile samples are cold-deformed, which means an increase in dislocation density, before testing. With respect to the starting value of pure bcc iron ($E = 210$ GPa), a reduced Young's modulus of 192 to 200 GPa was measured with respect to the strain state. If these results are transferred to fcc iron having a Young's modulus of 190 to 200 GPa in the uninfluenced condition, a reduced Young's modulus of 176 to 180 GPa will be the result. However, it should be emphasized here that the deformability of fcc-iron, the formation of dislocations, and the interactions of the dislocation with one another cannot be compared with those of bcc iron.

Eshelby et al. also found a decrease in material stiffness if the dislocation density increases [55]. This problem was treated theoretically by Koehler and de Wit for pinned dislocations in fcc crystals. They found a relationship between the change in the Young modulus ($\frac{\Delta E}{E}$), the dislocation density ρ , and the average loop length of the dislocation L , as shown in Eq. 3 ($K = \text{constant}$).

$$\frac{\Delta E}{E} = -K\rho L^2 \quad (3)$$

Young's modulus is decreased because reversible dislocation movements cause a reversible elastic expansion contribution to the total elongation. For this reason, the total strain is increased for a given stress, which is associated with a lower elastic stiffness [56]. Furthermore, it has to be taken into account that the cell-like substructure can be considered two separate structural constituents with different material properties due to differences in the respective chemical composition. The shell of the microcells is enriched in the element Mo, but the core of the cell is low in Mo. The influence of dislocation density and Mo segregation on a drop in the Young modulus was demonstrated indirectly on heat-treated samples. The Bh-HT samples were built horizontally using SLM device B and the optimized parameters. In addition, specimens were heat-treated in a hot isostatic press for 3 h at a temperature of 1150 °C, slowly cooled to room temperature, and then solution-annealed at 1000 °C in an inert-gas furnace (see [43]). Subsequent tensile tests on these heat-treated specimens confirm an increase in the Young modulus from 165 to approximately 205 GPa. Quantitative microstructural investigations on the Bh-HT samples clarify that the porosity could not be reduced by HIP treatment (see Table 4). This is due to the low solubility of the argon used as the process gas during SLM, as described in [44]. In addition, the core/shell-like substructure diminishes during HIP treatment, thus indicating diffusion processes, which is accompanied by a homogeneous distribution of all elements across the microstructure. In addition, the HIP process could also close existing cracks so that an increase in the Young modulus can be discussed with respect to a reduced dislocation density, a homogeneous distribution of the elements, and a crack-free microstructure.

Another characteristic of the mechanical properties of the investigated SLM-built specimens is the smaller values of the uniform elongation and the elongation at fracture compared with the cast reference material. The elongation values found in this work vary in a large range and correlate with the porosity. Thus, the sample with the highest porosity has the lowest elongation at fracture of 15.5%, which corresponds to approximately one-quarter of the elongation at fracture of the cast reference specimen ($A = 69 \pm 9\%$). These low elongation

values in combination with the determined strength values are associated with a low specific fracture energy of 80 to 208 J/cm². In contrast, the specific fracture energy of the reference sample in the cast condition is about 361 J/cm². Thus, all determined specific fracture energies of the SLM-manufactured samples are below that of the cast reference specimen, which is a result of the low elongation at fracture. Improved elongation at fracture of SLM-manufactured specimens can be reached by reducing the sample's porosity, which can be achieved by optimizing the scanning strategy, the build-up direction, a multiple local heat input, and a post-treatment in the form of a HIP process [57–59]. Although it has been impressively demonstrated in other works that post-treatment, such as hot-isostatic pressing, improves the elongation at fracture and the fatigue properties [60] of SLM-manufactured components, the strength, in particular the yield strength, drops [43]. The decrease in yield strength can be attributed to a reduction in the dislocation density because of microstructural annealing processes and grain growth of the substructure. The

strength-increasing effect of the substructure, according to the Hall-Patch relationship, is thus lost. In summary, SLM-built components have a higher strength than cast components, but they also have a lower elongation at fracture, promoting a failure at lower strain.

Figure 6 depicts the fractured surface of all specimens. The fractured surface of the tensile specimens shows clear evidence of a ductile fracture, as indicated by a dimpled surface. If isolated defects, such as pores, can be registered in the fractured surface of the samples produced with SLM devices A and D, the B and C specimens exhibit clear defects, such as cavities and brittle failure, which is characterized by a cleavage fracture. Sample B has large pores up to a size of 50 μm, which significantly define the material failure under tensile load. The fracture surface of sample B exhibits a higher defect density (pores, cavities, cracks) than initially measured in the cross-section of the samples using quantitative image analysis. The higher defect density in the fracture surface in contrast to the cross-section of the microstructure can be explained by the

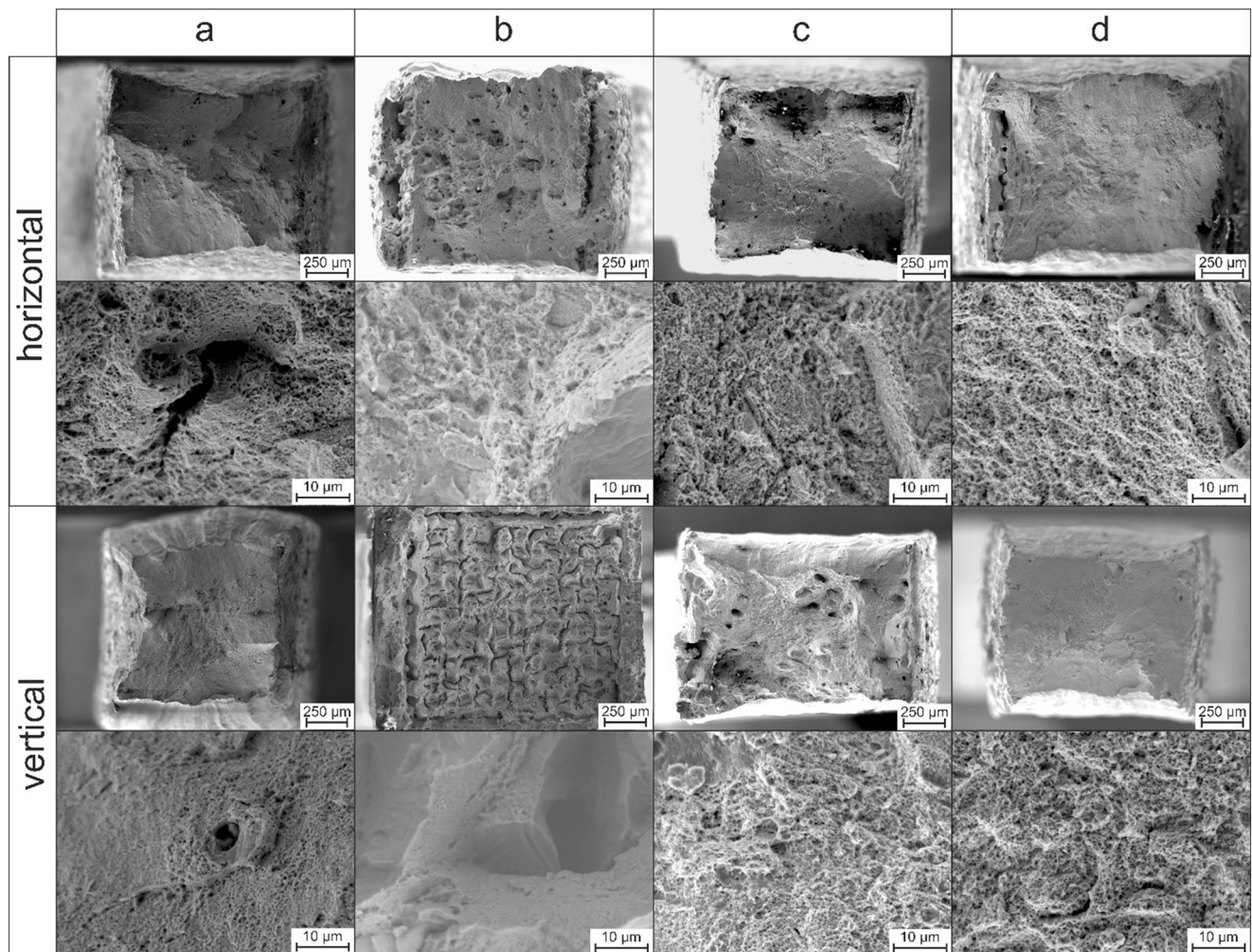


Fig. 6 Characteristic fracture surfaces of the tensile specimens depending on build-up direction and SLM device

crack propagation during failure in the tensile test. The crack propagation does not take place perfectly perpendicular to the stress direction. Instead, the crack is frequently deflected by microstructural defects, which leads to a fracture surface with a high roughness. For this reason, not only the porosity defines the material behavior but also the distribution of the pores in the microstructure and their morphology should be considered. Thus, as the specimens manufactured using SLM machine B show, a porosity of less than 1% in a randomly measured cutting plane can have an effect similar to a porosity of 3 to 5%, for example, when the pores are close to each other and promote crack propagation. Thus, the porosity values determined by quantitative image analysis should be interpreted with caution since they do not correctly reflect the actual effect of the pores.

3.4 Statistical analysis of materials properties of SLM-manufactured 316L stainless steel specimens

The results presented above confirm that the SLM-manufactured specimens differ significantly from the cast reference specimen in terms of their mechanical properties and the scattering of the strength and elongation values. In some cases, a clear relation cannot be mapped between the SLM device, the build-up direction, and the determined porosity. All measured values are therefore characterized by a relatively high standard deviation, indicating that the failure of SLM-manufactured components is determined by the biggest defect in the structure, analogously to ceramic materials. For this reason, the scale parameter and the Weibull modulus m were determined based on all measured values with respect to the build-up direction and independent of the SLM device. The scale parameter is defined here as the measured value at which 63.2% of the respective strength ($\sigma_{0Rp0.2}$, σ_{0Rm}) or elongation (A_{G0} , A_0) was present, taking into account all measured values with respect to the respective built-up

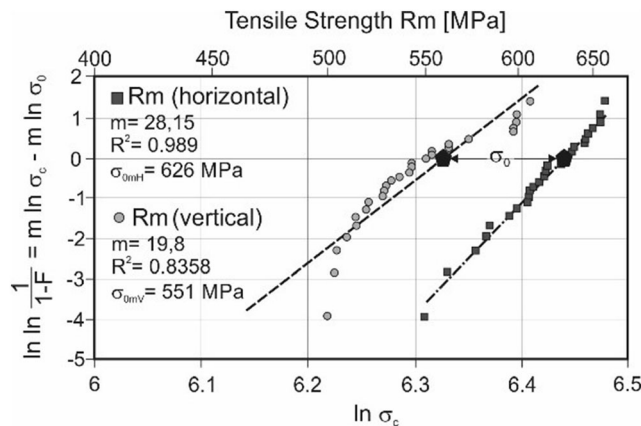


Fig. 7 Evaluation and determination of the mean tensile strength and the Weibull modulus depending on the build-up direction

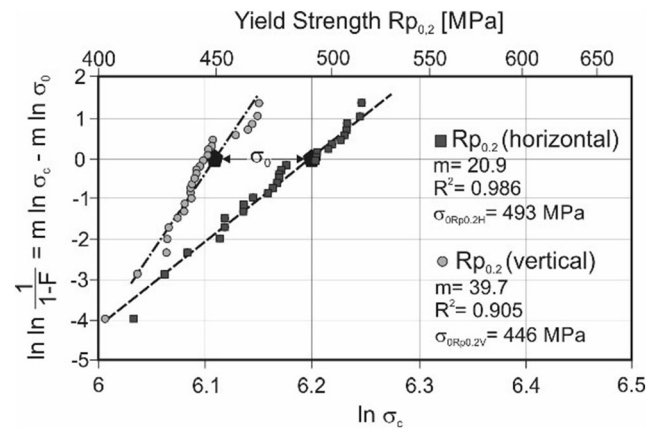


Fig. 8 Evaluation and determination of the mean yield strength and the Weibull modulus depending on the build-up direction

direction of the samples. To obtain sufficient statistics, a total of 47 tensile tests were carried out. The idea of this approach is to provide meaningful values that can then be used in the constructive design of SLM-manufactured components.

The Weibull distribution of all measured tensile strengths as a function of the build-up direction is shown in Figs. 7, 8, 9, and 10, and the respective characteristic values are listed in Table 5. A Weibull coefficient of $m = 19.8$ (vertical) and $m = 28.15$ (horizontal) and a medium tensile strength of 551 MPa (vertical) and 626 (horizontal) were determined. In contrast, the Weibull coefficient of $m = 37.56$ and a medium tensile strength of 604 MPa of the cast reference sample were calculated. It can be clearly seen from Fig. 7 that the slope of both graphs is slightly different, which corresponds to the different Weibull coefficients. However, the fit line of the tensile samples with horizontal build-up is linearly shifted towards a higher tensile strength. The results of the yield strength are given in Fig. 8. The average yield strengths of the horizontally and vertically built samples are close to each other and can be specified with $R_{p0.2h} = 493$ and $R_{p0.2v} = 446$ MPa. Differences can be clearly seen in the

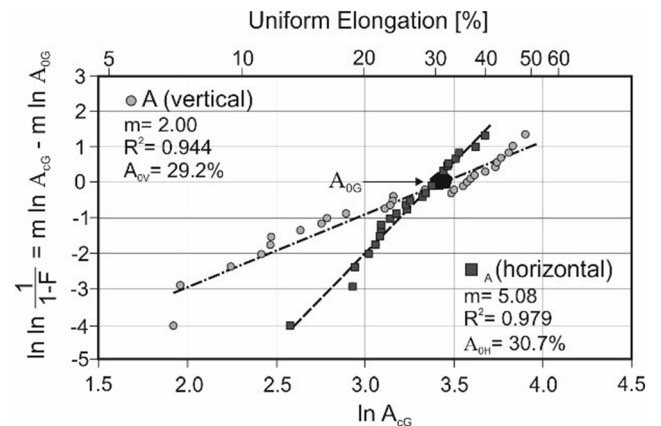


Fig. 9 Evaluation and determination of the mean uniform elongation and the Weibull modulus depending on the build-up direction

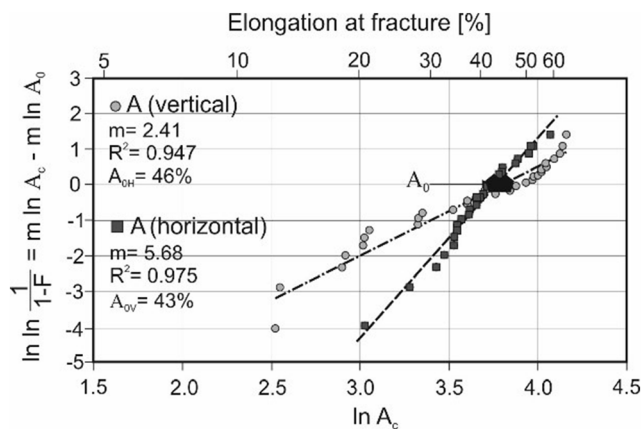


Fig. 10 Evaluation and determination of the mean elongation at fracture and the Weibull modulus depending on the build-up direction

slope of the fit curve, i.e., in the Weibull modulus. The Weibull modulus of horizontally built samples was calculated to be $m = 39$ and is thus twice as high as the Weibull modulus of the vertically built samples ($m = 20.9$). In contrast, the Weibull modulus of the yield strength determined for the cast reference is $m = 16.54$ at an average strength of 383 MPa. This result shows that the 316L material processed by SLM has a reproducible yield strength compared with the same material in the cast condition. In addition, the average mean of the yield strength is less affected by the build-up direction. A completely different situation arises for the measured uniform elongation (Fig. 9) and the elongation at fracture (Fig. 10). As a characteristic, the respective elongation values for horizontally built specimens ($A_{gh} = 31\%$; $m = 5.08$) possess a higher Weibull modulus compared with the samples built vertically ($A_{gv} = 29\%$; $m = 2.00$). The average value for the calculated uniform elongation is at the same level.

This result again impressively illustrates the effect of microstructural defects that unfold their maximum negative effects when the samples are subjected to a load perpendicular to the layered structure. An analogous behavior can be deduced from the results of the elongation at fracture. The horizontally built samples have a higher elongation at fracture and a higher Weibull modulus of $m = 5.68$ in comparison to the vertically built samples ($m = 2.41$).

However, it should be expressly pointed out that the mean values given in Table 5 represent a temporary

impression of the current process technology. It is assumed that both the mean values for strength, elongation, and the Weibull modulus will increase in future because of ongoing optimization (powder feeding, applying of a dense and homogeneous powder layer, energy insertion and powder-melting) of SLM technology. Thus, we assume that the values of the cast reference material, especially the Weibull modulus, will be reached in the future. Furthermore, it must be mentioned at this point that the determined mechanical mean values and Weibull moduli apply to the tested volume of the tensile specimen. Since the possibility of a fracture-determining defect increases with the component's volume, the Weibull modulus is likely to drop with increasing component volume. This question should be validated in subsequent research on different-sized tensile specimens. The low material properties and the small Weibull modulus for the strain values, especially in the vertically built specimens, could be mainly attributed to powder feeding. Especially binding defects between two adjacent layers and large pores, which are isolated in the microstructure, might be attributed, inter alia, to a locally insufficient powder bed density. In order to minimize microstructural defects, further measures must be taken to ensure a homogeneous powder distribution with high bulk density. In particular, during the production of specimens using the SLM device B, no homogeneous powder layer was applied because of the radial movement of the recoater, which is considered the main reason for the relatively high specimen porosity. Thus, there are possibilities for optimization both in the powder layer application and in the optimization of the starting powder. With regard to powder optimization, powders having less satellites and multimodal distribution should be used to ensure a powder layer with a high bulk density and a good flowability.

4 Conclusions

This work investigated the influence of different SLM devices on the microstructure and the resulting material properties. The steel powder from the same powder

Table 5 Estimated average values of the mechanical properties and the associated Weibull modulus

Building direction	Yield strength, $R_{P0.2}$ [MPa]	Weibull modulus for yield strength	Tensile strength, R_m [MPa]	Weibull modulus for tensile strength	Ultimate elongation, A_g [%]	Weibull modulus of ultimate elongation	Elongation at fracture A [%]	Weibull modulus for elongation at fracture
Horizontal	493	20.90	626	28.15	31	5.08	43	5.68
Vertical	446	39.70	551	19.80	29	2.00	46	2.41
Cast reference	384	16.54	604	37.56	50	15.66	66	14.89

batch was used for all tests so that only the influence of the different SLM machines becomes visible. Tensile specimens were produced horizontally and vertically and the microstructure and tensile properties were compared. From the obtained results, the following conclusions can be drawn. The SLM-built austenitic stainless steel AISI 316L possesses a hierarchical microstructure. The microstructure consists of grains with a size of 10–50 μm and fine subgrains within single grains. No significant influence of the employed SLM machines on the microstructure was observed, which indicates similar thermal conditions during each build-cycle. However, specimens built using different SLM machines were found to have a considerably different porosity. Pronounced differences in terms of mechanical strength were detected between the specimens produced on the four employed SLM devices, although optimized process parameters were used for each individual device. Therefore, the influence of different SLM devices has to be taken into account when producing structural parts. In this context, the influence of the powder supply system appears to be important and has thus to be investigated more deeply in the future. The SLM-manufactured specimens possess a tensile strength which is at least as high or higher than the cast reference material. The yield strength of the SLM-manufactured specimens exceeds that of the cast material, which is due to the small cell size of the substructure and the resulting increase in yield strength according to the Hall-Petch relationship. Another characteristic is the lower Young's modulus of SLM-manufactured specimens in contrast to the cast reference, which is attributed to a higher dislocation density and a pronounced core/shell substructure. The properties of SLM-manufactured components are essentially defined by the defect density, analogously to ceramic components. In contrast to the uniform elongation A_g and the elongation at fracture, the defect density less influences the materials strength. Based on the performed measurements, the Weibull coefficient m and the respective average strength and elongation values were determined, which underline the aforementioned statements. In future investigations, especially the influence of the specimen size on the Weibull modulus has to be investigated. Further research is required with regard to the influence of the recoater system, the characterization of the applied powder layers (local packing density, reusability of powders, homogeneity) and the influence of further post processing (heat treatment, HIP post-compression) on the mechanical, chemical, and cyclical material properties. There is also the question of whether the results obtained for 316L stainless steel can be transferred to other material systems.

Acknowledgments The authors gratefully acknowledge the support by the Deutsche Edelstahlwerke GmbH for providing the steel powder for our investigations.

Funding Open access funding provided by Projekt DEAL.

Data availability The authors can confirm that all relevant data are included in the paper. Raw data available on request from the corresponding author.

Open Access This article is licensed under a Creative Commons Attribution 4.0 International License, which permits use, sharing, adaptation, distribution and reproduction in any medium or format, as long as you give appropriate credit to the original author(s) and the source, provide a link to the Creative Commons licence, and indicate if changes were made. The images or other third party material in this article are included in the article's Creative Commons licence, unless indicated otherwise in a credit line to the material. If material is not included in the article's Creative Commons licence and your intended use is not permitted by statutory regulation or exceeds the permitted use, you will need to obtain permission directly from the copyright holder. To view a copy of this licence, visit <http://creativecommons.org/licenses/by/4.0/>.

References

1. Frazier EE (2014) Metal additive manufacturing: a review. *JMEPEG* 23:1917–1928
2. Huang R, Riddle M, Graziano D, Warren J, Das S, Nimbalkar S, Cresko J, Masanet E (2016) Energy and emission saving potential of additive manufacturing: the case of lightweight aircraft components. *J Clean Prod* 135:1559–1570
3. Ford S, Despeisse M (2016) Additive manufacturing and sustainability: an exploratory study of the advantages and challenges. *J Clean Prod* 137:1573–1587
4. Conner B. P., Manogharan G. P., Martof A. N., Rodomsky L. M., Rodomsky C. M., Jordan D. C., Limperos J. W.: Making sense of 3-D printing: creating a map of additive manufacturing products and services, *Additive Manufacturing*, 1–4 (2014), pp. 64–74
5. Körner C (2016) Additive manufacturing of metallic components by selective electron beam melting – a review. *Int Mater Rev* 61(5): 361–377
6. Olakanami EO, Chochrane RF, Dalgarno KW (2015) A review on selective laser sintering/melting (SLS/SLM) of aluminium alloy powders: processing, microstructure, and properties. *Prog Mater Sci* 74:401–477
7. Liverani E, Toschi S, Ceschni I, Fortunato A (2017) Effect of selective laser melting (SLM) process parameters on microstructure and mechanical properties of 316L austenitic stainless steel. *J Mater Process Technol* 249:255–263
8. Yadroitsev I, Krakhmalev P, Yadroitsava I, Johansson S, Smurov I (2013) Energy input effect on morphology and microstructure of selective laser melting single track from metallic powder. *J Mater Process Technol* 213:606–613
9. Yadollahi A, Shamsaei N, Thompson SM, Seely DW (2015) Effects of process time interval and heat treatment on the mechanical and microstructural properties of direct laser deposited 316L stainless steel. *Mater Sci Eng A* 655:171–183
10. Wauthle R, Vrancken B, Bexnaerts B, Jorisson K, Schrooten J, Kruth JP, Humbeek JV (2015) Effects of building orientation and heat treatment on the microstructural and mechanical properties of selective laser melted Ti6Al4V lattice structures. *Additive Manufacturing* 5:77–84
11. Utela B, Storti D, Anderson R, Ganter M (2008) A review of process development steps for new material system in three dimensional printing (3DP). *J Manuf Process* 10-2:96–104

12. Qiu C, Panwisawas C, Ward M, Basoalto HC, Brooks JW, Attallah MM (2015) On the role of melt flow into the surface structure and porosity development during selective laser melting. *Acta Mater* 96:72–79
13. Yang Y, van Keulen F, Ayas C (2020) A computationally efficient thermal model for selective laser melting. *Additive Manufacturing* 31:100955
14. Haeri S., Wang Y., Ghita O., Sun J.: Discrete element simulation and experimental study of powder spreading process in additive manufacturing
15. Du Y, You X, Qiao F, Guo L, Liu Z (2019) A model for predicting the temperature field during selective laser melting. *Results in Physics* 12:52–60
16. Tang M, Pistorius PC, Beuth JL (2017) Prediction of lack-of-fusion porosity for powder bed fusion. *Additive Manufacturing* 14:39–48
17. Ning J, Wang W, Zamorano B, Liang SY (2019) Analytical modeling of lack-of-fusion porosity in metal additive manufacturing. *Applied Physics A* 125:797
18. Ning J, Sievers DE, Garmestani H, Liang SY (2020) Analytical modeling of part porosity in metal additive manufacturing. *Int J Mech Sci* 172:105428
19. Zhang Y, Zhang J (2019) Modeling of solidification microstructure evolution in laser powder bed fusion fabricated 316L stainless steel using combined computational fluid dynamics and cellular automata. *Additive Manufacturing* 28:750–765
20. Vandenbroucke B., Kruth J.-P.: Selective laser melting of biocompatible metals for rapid manufacturing of medical parts, *Rapid Prototyping Journal*, Vol. 13 Issue: 4 (2007), pp.196–203,
21. Mertens A., Reinster S., Contrepolis Q., Dormal T., Lemaire O., Lecomte-Beckers J.: Microstructure and mechanical properties of stainless steel AISI 316L processed by selective laser melting, published in *Materials Science Forum*, 783–786 (2014), pp. 898–903
22. Delgado J., Ciurana J., Rodriguez C. A.: Influence of process parameters on part quality and mechanical properties for DMLS and SLM with iron-based materials; *International Journal of Advanced Manufacturing Technology*, 60, Issue 5-8, (2012), pp. 601–610
23. Rasch M., Huber F., Butzhammer L., Merz C., Schmidt M.: Effect of scanning sequence on subsurface porosity at laser beam melting in powder bed, *Proceedings of the 14th Rapid. Tech Conference, Trade Forum AM science*, (2017), pp. 255-268
24. Löber L, Flache C, Petters R, Kühn U, Eckert J (2013) Comparison of different post processing technologies for SLM generated 316L steel parts. *Rapid Prototyp J* 19(3):173–179
25. Casati R., Vedani L. M.: Microstructure and fracture behavior of 316L austenitic stainless steel produced by selective laser melting, *Journal of Materials Science and Technology*, 32, Issue 8,(2016), pp. 738–744
26. Fischmeister H. F., Ozerski A. D., Olsson L.: Solidification structure of gas-atomized high-speed steel powders, *Powder Metallurgy*, 25:1, 1–9 (1982)
27. Wang D, Song C, Yang Y, Bai Y (2016) Investigation of crystal growth mechanism during selective laser melting and mechanical property characterization of 316L stainless steel parts. *Mater Des* 100:291–299
28. Hengsbach F., Koppa P., Holzweissig M. J., et al.: Inline additively manufactured functionally graded multi-materials. Microstructure and mechanical characterization of 316L parts with H13 layers, *Progress in Additive Manufacturing*, (2018), pp. 1–9
29. Prashanth KG, Eckert J (2017) Formation of metastable cellular microstructures in selective laser melted alloys. *J Alloys Compd* 707:27–34
30. Zhong Y, Liu L, Wikman S, Cui D, Shen Z (2016) Intergranular cellular segregation network structure strengthening 316L stainless steel prepared by selective laser melting. *J Nucl Mater* 470:170–178
31. Birnbaum AJ, Steuben JC, Barrick EJ, Iliopoulos AP, Michopoulos JG (2019) Intrinsic strain aging, Σ 3 boundaries, and origins of cellular substructure in additively manufactured 316L. *Additive Manufacturing* 29:100784
32. Saeidi K, Gao X, Zhong Y, Shen ZJ (2015) Hardened austenite steel with columnar subgrain structure formed by laser melting. *Mater Sci Eng A* 625:221–229
33. Ning J, Sievers DE, Garmestani H, Liang SY (2019) Analytical modeling of in-process temperature in powder bed additive manufacturing considering laser power absorption, latent heat, scanning strategy, and powder packing. *Materials* 12:808
34. Boes J, Röttger A, Mutke C, Escher C, Theisen W (2018) Microstructure and mechanical properties of X65MoCrWV3-2 cold-work tool steel produced by selective laser melting. *Additive Manufacturing* 23:170–180
35. Yusuf SM, Chen Y, Boardman R, Yang S, Gao N (2017) Investigation on porosity and microhardness of 316L stainless steel fabricated by selective laser melting. *Metals* 64(7):2–12
36. Sander GM, Thomas S, Cruz V et al (2017) On the corrosion and metastable pitting characteristics of 316L stainless steel produced by selective laser melting. *J Electrochem Soc* 164(6):250–257
37. Yi H., Qi L., Luo J., Jiang Y., Deng W.: Pinhole formation from liquid metal microdroplets impact on solid surfaces, *Appl. Phys. Lett.* 108 (2016)
38. Ferrar B, Mullen L, Jones E, Stamp R, Sutcliffe CJ (2012) Gas flow effects on selective laser melting (SLM) manufacturing performance. *J Mater Process Technol* 212:355–364
39. Matthews MJ, Guss G, Khairallah SA, Rubenchik AM, Depond PJ, King WE (2016) Denudation of metal powder layers in laser powder bed fusion processes. *Acta Mater* 114:33–42
40. Yadroitsev I, Bertrand P, Smurov I (2007) Parametric analysis of the selective laser melting process. *Appl Surf Sci* 253:8064–8069
41. Ali U, Mahmoodkhani Y, Imani Shahabad S, Esmailizadeh R, Liravi F, Sheydaeian E, Huang KY, Marzbanrad E, Vlasea M, Toyserkani E (2018) On the measurement of relative powder-bed compaction density in powder-bed additive manufacturing processes. *Mater Des* 155:495–501
42. Mahmoodkhani Y, Ali U, Imani Shahabad S, Rani Kasinathan A, Esmailizadeh R, Keshavarzkermani A, Marzbanrad E, Toyserkani E (2019) On the measurement of effective powder layer thickness in laser powder-bed fusion additive manufacturing of metals. *Prog Addit Manuf* 4:109–116
43. Röttger A, Geenen K, Binner F, Theisen W (2016) Comparison of microstructure and mechanical properties of 316L austenitic steel processed by selective laser melting with hot-isostatic pressed and cast material. *Mater Sci Eng A* 678:365–376
44. Geenen K., Röttger A., Theisen W. (2017) Corrosion behavior of 316L austenitic steel processed by selective laser melting, hot-isostatic pressing, and casting, *Mater Corros* 68:7 (2017), pp. 764–775
45. Deev AA, Kuznetsov PA, Petrov SN (2016) Anisotropy of mechanical properties and its correlation with the structure of the stainless steel 316L produced by the SLM method. *Phys Procedia* 83: 789–796
46. Merkt SJ (2015) Qualifizierung von generativ gefertigten Gitterstrukturen für maßgeschneiderte Bauteilfunktionen, Ph.D. Thesis, RWTH Aachen, Aachen, Germany
47. Hitzler L, Hirsch J, Heine B et al (2017) On the anisotropic mechanical properties of selective laser melted stainless steel. *Materials* 10:1136
48. Niendorf A, Leuders S, Riemer A, Richard HA, Tröster T, Schwarze D (2013) Highly anisotropic steel processed by selective laser melting. *Metall Mater Trans B* 44B:794–796
49. Sun Z, Tan X, Tor SB, Chua CK (2018) Simultaneously enhanced strength and ductility for 3D-printed stainless steel 316L by selective laser melting. *NPG Asia Materials* 10:127–136

50. Losertová M, Kubes V (2017) Microstructure and mechanical properties of selective laser melted Ti6Al4V alloy, IOP conference series, materials science and engineering, 266
51. Capek J., Machová M., Fousová M., Kubásek D. et al.: Highly porous, low elastic modulus 316L stainless steel scaffold prepared by selective laser melting, *Materials Science Engineering C Biol. Appl.*, 69 (2016), pp. 631–639
52. Joguet D, Danlos Y, Bolot R, Montavon G, Coddet C (2014) Modeling and measurement of effective Young modulus of porous biomedical materials manufactured via SLM. *Key Eng Mater* 606: 125–128
53. Saeidi K, Akthar F (2018) Subgrain-controlled growth in the laser-melted 316L promoting strength at high temperatures. *R Soc Open Sci* 5:172394
54. Benito JA, Jorba J, Manero JM, Roca A (2005) Change of Young's modulus of cold-deformed pure iron in a tensile test. *Metall and Mat Trans A* 36:3317–3324
55. Eshelby JD, Mott NF (1949) Dislocations as a cause of mechanical damping in metals. *Proc R Soc Lond A* 197:396–416
56. Koehler JS, DeWit G (1959) Influence of elastic anisotropy on the dislocation contribution to the elastic constants. *Phys Rev* 116: 1121–1125
57. Wang D, Yang Y, Su X, Chen Y (2012) Study on energy input and its influences on single-track, multi-track, and multi-layer in SLM. *Int J Adv Manuf Technol* 58:1189–1199
58. Popovich VA, Borisov EV, Popovich AA, Sufiiarov VS, Massaylo DV, Alzina L (2017) Impact of heat treatment on mechanical behavior of Inconel 718 processed with tailored microstructure by selective laser melting. *Mater Des* 131:12–22
59. Mertens R, Clijsters S, Kempen K, Jruth J-P (2014) Optimization of scan strategies in selective laser melting of aluminium parts with downfacing areas. *J Manuf Sci Eng* 136:6
60. Riemer A, Leuders S, Thöne M, Richard HA, Tröster T, Niendorf T (2014) On the fatigue crack growth behavior in 316L stainless steel manufactured by selective laser melting. *Eng Fract Mech* 120:15–25

Publisher's note Springer Nature remains neutral with regard to jurisdictional claims in published maps and institutional affiliations.